In-situ growth of Fe/Fe₃O₄/C hierarchical architectures with wide-band electromagnetic wave absorption

Xiaohuan Meng[a,1], Jian Zhang[a,1], Li Xiong[a], Tao Zhang[a,*], Hu Zhao[b], Bo Zhong[a], Long Xia[a], Xiaoxiao Huang[c], Guangwu Wen[c,d]

[a] School of Materials Science and Engineering, Harbin Institute of Technology (Weihai), Weihai 264209, PR China
[b] School of Materials, University of Manchester, Oxford Road, Manchester M13 9PL, UK
[c] School of Materials Science and Engineering, Harbin Institute of Technology, Harbin 150001, PR China
[d] School of Materials Science and Engineering, Shandong University of Technology, 255049, PR China

ABSTRACT

Carbon materials have aroused extensive interests for their remarkable electrical properties as electromagnetic wave (EMW) absorption. However, the synthesis of the wide-band electromagnetic wave absorbent is an insuperable challenge for attaining effective refection loss and electromagnetic matching. Herein, a facile method for large-scale synthesis of monodispersed Fe/Fe₃O₄/C composite microspheres is proposed. The carbon microspheres (1–2 μm in diameter) imbedded with nanosized Fe/Fe₃O₄ particles (10–20 nm) are uniformly produced by polymerization and carbothermic reduction processes. The products exhibit the minimum refection loss −45.5 dB at 9.4 GHz and a broad bandwidth of 4.1 GHz below −10 dB from 7.8 GHz to 11.9 GHz with a thickness of 3.0 mm. The absorption mechanism indicates a unique deviated Debye dipolar relaxation effect in the absorbing bandwidth.

1. Introduction

The extensive utilization of electronic devices and wireless equipment in civil and military fields has resulted in serious electromagnetic radiation pollution, which has harmful effects on human body and electronic apparatus [1–3]. Therefore, the effective electromagnetic wave (EMW) absorption materials are urgently designed and explored [4]. The EMW absorption materials is composed of dielectric and magnetic materials such as carbonaceous materials and ferrite materials, respectively [5]. The absorption of EMW is achieved by the attenuation of incident EMW energy through electromagnetic impedance matching (Z_{in}/Z_0), magnetic loss (μ_r) and dielectric loss (ε_r) [6–8]. Hence, the three factors (Z_{in}/Z_0, μ_r and ε_r) determine the absorption capability of the absorbents. A perfect impedance matching ($Z_{in}/Z_0 = 1$) indicates the incident EMW could achieve zero reflection at the front surface of the absorbent [9]. Hence, a perfect impedance matching between the absorbent and the incident EMW is critical for enhancing EMW absorption [10]. The coefficient of impedance matching can be described as follows [11]:

$$Z_{in}/Z_o = \sqrt{\mu_r/\varepsilon_r}\tanh[j(2\pi fd/c\sqrt{\mu_r\varepsilon_r})] \qquad (1)$$

According to the transmission line theory, the reflection loss (RL) can be expressed as below [12]:

$$RL = 20\log\left|\frac{Z_{in} - Z_o}{Z_{in} + Z_o}\right| \qquad (2)$$

where, $\mu_r = \mu' + i\mu''$ and $\varepsilon_r = \varepsilon' + i\varepsilon''$ are the complex permeability and permittivity of the absorbent, respectively. μ' and μ'' are the real part and imaginary part of permeability, respectively. ε' and ε'' are the real part and imaginary part of permittivity, respectively.

Pure carbon architectures, such as carbon nanotubes [13–15] and graphene [16,17], not only have high surface area and excellent conductivity but also exhibit intensive absorption at GHz level [18–20]. However, the absorption bandwidth of these carbon architectures cannot be satisfied due to the absence of magnetic loss [21]. Moreover, the poor flowability and dispersibility of the carbon nanotubes and graphene limit their use due to the difficulty for piping and praying to gain a uniform stealth coating. Hence, spherical carbon architectures decorated with functional nanoparticles is critical to obtain effective EMW absorption and good flowability for large scale applications.

Ferrite materials such as Fe₃O₄, have been extensively used in EMW absorption due to their superior magnetic loss property [22–24]. Large

---
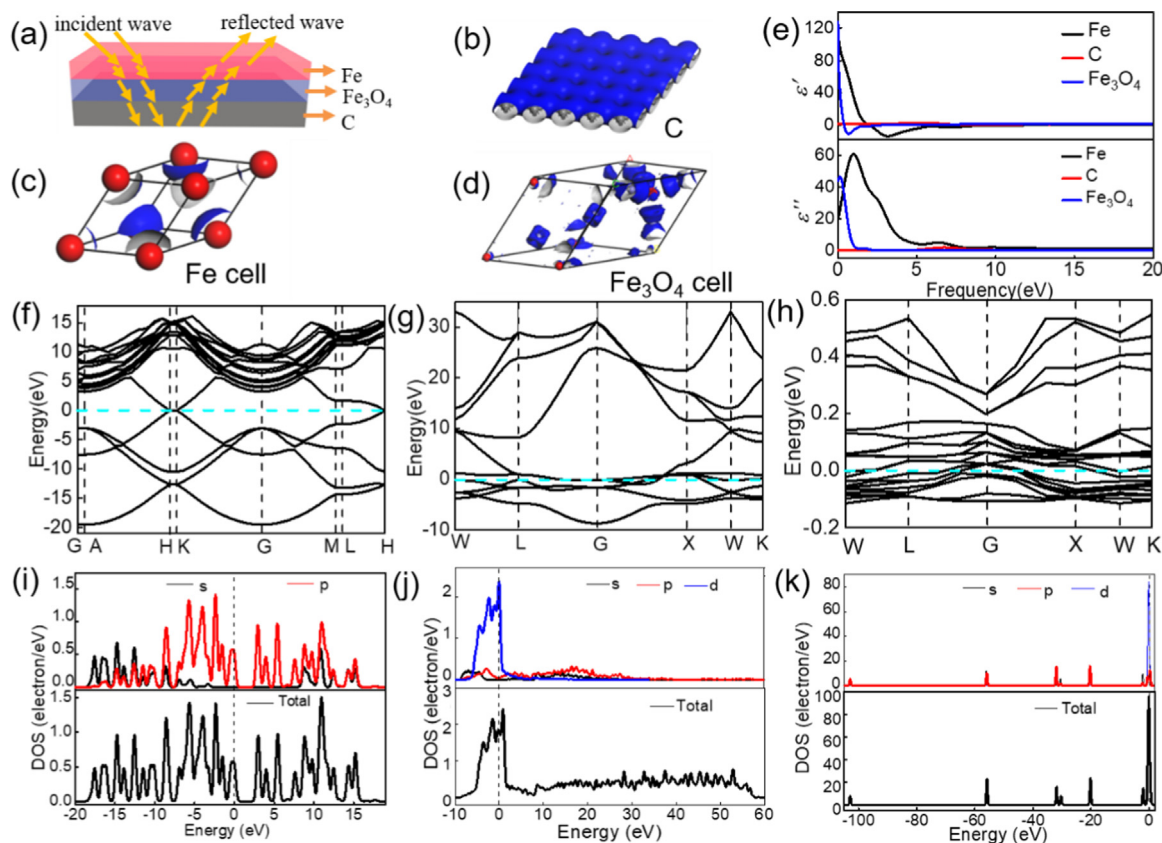
Fig. 1. (a) Schematic illustration of EMW absorption in the composite. Calculation the performance of EMW absorption by CASTEP. the electron density of (a) the carbon, (b) Fe cell, (c) Fe_3O_4 cell; (e) the real (ε′) and imaginary (ε″) part of the complex permittivity of carbon, Fe cell and Fe_3O_4 cell, respectively; (f–h) band structure and (i–k) DOS of carbon, Fe cell and Fe_3O_4 cell, respectively.

numbers of literatures in relation to various ferrite composites for EMW absorption have been reported. For example, Hosseini et al. reported that the PANI/$MnFe_2O_4$ nanocomposites have excellent absorbing properties, with a wide bandwidth about 6.9 GHz and minimum reflection loss of −15.3 dB at 10.4 GHz at the thickness of 1.4 mm [25]. Sun et al. researched the EMW absorption of the Fe_3O_4@ZnO spheres decorated graphene, and reported a minimum reflection loss of −40 dB [26]. Li et al. studied the EMW absorbing properties of the Fe_3O_4@C core-shell nanotubes, and the results showed that the minimum reflection loss was −22.6 dB at 16.2 GHz with a bandwidth of 6 GHz [27]. Liu et al. reported the EMW absorption properties of the Fe_3O_4/SiO_2 nanorods and polyvinylidene fluoride, and the results exhibited the minimum reflection loss reached to −28.6 dB at 8.1 GHz with the thickness of 2.5 mm [28]. Although all of the above reported works have focused on the EMW absorption of carbon/ferrite based absorbents, the exploration for lightweight architectures possessing strong absorption, broad bandwidth and good flowability and dispersibility is still a challenge for large scale stealth coating applications.

Herein, we propose a facile approach through pyrolysis of polystyrene (PS) modified by Fe^{3+} to fabricate the Fe/Fe_3O_4/C monodispersed composite microspheres to improve the impedance matching for enhanced EMW absorption. Effects of the concentration of styrene monomer on the microstructural morphologies and crystalline structure of the as-prepared Fe/Fe_3O_4/C are studied in detail. Additionally, obvious EMW dielectric dispersion effect and deviated Debye dipolar relaxation effect are discussed. These findings point to important guidelines to take advantages of functionalized carbon-based absorber and pave the road for the development of a large family of novel EMW absorbents.

2. Experimental

2.1. Syntheses of the Fe/Fe_3O_4/C monodispersed composite microspheres

Considering the monodispersed spherical morphology of the organic PS particles, a totally new synthesis route is artfully designed by pyrolyzing a simple precursor to obtain an enhanced EMW absorbent which can be synthesized in large scale. A three-layered carbon architecture including Fe_3O_4, Fe and carbon layer was designed. The monodispersed carbon microspheres function as the conductive substrate. Fe and Fe_3O_4 function as the impedance matching layer and magnetic loss layer, respectively.

The PS emulsion was prepared through a method of soap-free emulsion polymerization, the advantages of which are the fast polymerization rate, the uniform particle size and the short reaction time. Firstly, styrene (20 vol% , analytical reagent, from Tianjin Kaixin Chemical Co., Ltd) was added to a three-necked flask contained 500 mL deionized water and then the mixed solution was stirred mechanically for 10 min in a thermostatic water bath (70 °C) to remove the dissolved oxygen. Then, the initiator ammonium persulfate (2.5 wt%, analytical reagent, from Shanghai Zhongkehang Chemical Co., Ltd) was added into the above solution and kept stirring for 24 h at the rotation speed of 400 r/min in a magnetic stirring heating device. The PS emulsion was generated and ready for immediate use.

The Fe_3O_4 nanoparticles were prepared by a coprecipitation method. At first, the $FeCl_3$·$6H_2O$ (10 wt%, analytical reagent, from Shanghai Zhanyun Chemical Co., Ltd.) was dispersed in deionized water in a three-necked flask with the protection of flowing nitrogen (30 mL/min with a purity of 99.999%). Subsequently, $FeCl_2$·$6H_2O$ (the molar ratio Fe^{3+}:Fe^{2+} = 4:3, analytical reagent, from Shanghai Zhanyun Chemical Co., Ltd.) and a small amount of surfactant sodium

dodecyl sulfonate (0.2 wt% , analytical reagent, from Shanghai Chemical Co., Ltd) were added rapidly into the three-necked flask under the protection of N_2 atmosphere. After that, ammonia water (20 wt%, 0.91 g/cm^3, analytical reagent, Laiyang economic and technological development zone.) was added into the solution to adjust pH value to 9.5 and the color of the solution turned black quickly when Fe_3O_4 nanoparticles were precipitated.

The schematic illustration of EMW absorption mechanism of the composites is proposed in Fig. 1a. A ternary $Fe/Fe_3O_4/C$ composite microspheres was successfully designed , which can effectively attenuate the incident EMW. Under external alternating electromagnetic field, EMW energy was dissipated to transform into heat by the multi-layers structure induced eddy. To predict the performance of EMW absorption of carbon, Fe and Fe_3O_4, theorical calculation is implemented using the first-principles density functional theory (DFT) method in Crmbridge Sequential Total Energy Package (CASTEP) code of Materials Studio software 8.0 [29]. Ultrasoft pseudopotential is performed to obtain the more accurate optimization with the cutoff energy of the plane-wave of 300 eV and k-points of $1 \times 1 \times 1$. The electron density clouds of carbon, Fe and Fe_3O_4 are shown in Fig. 1b–d. The polarization of the electron density is increased from carbon, Fe to Fe_3O_4 respectively indicating that the hybrid structure of the $Fe/Fe_3O_4/C$ would promote the EMW absorption [30]. The simulated results of the complex permittivity ($\varepsilon_r = \varepsilon' + i\varepsilon''$) of carbon, Fe and Fe_3O_4 are exhibited in Fig. 1e. Planck-Einstein relation (E = hυ) describes the relationship of energy (E) and frequency (υ) of incident EMW, and h is the Plank constant. Fe and Fe_3O_4 have a higher ε' and ε'' than carbon at lower frequency, so the composites conjectured could have a better the performance of EMW absorption. Fig. 1f–h depicts the calculation data of band structure of carbon, Fe and Fe_3O_4, respectively. It is worth noting that the energy levels of carbon, Fe and Fe_3O_4 are very close to the Fermi level (the light blue dash), revealing the dominative hole-conductivity [31]. The total density of state (DOS) (underneath of Fig. 1i–k of carbon, Fe and Fe_3O_4, respectively) consists of partial density of state (PDOS) showing the curves of s, p and d orbits [32]. Near Fermi energy, the total orbit of carbon is occupied by p orbit and the total orbit of Fe and Fe_3O_4 is dominated by d orbit revealing the contributions of resonance absorption [33].

The imaginary part (ε'') of the complex permittivity is determined by the below equation [34]:

$$\varepsilon'' = \frac{\sigma_{dc}}{\omega \varepsilon_o} + \varepsilon_{ac}'' \tag{3}$$

where σ_{dc} is the direct current (DC) conductivity, ω is the angular frequency, ε_0 is the permittivity of free space, and ε_{ac}'' is the contribution of dielectric loss. According to the above analysis, the combination of carbon, Fe and Fe_3O_4 has the proper relative dielectric constant and relative magnetic permeability which would promotes the absorption of EMW, thereby the ternary composite $Fe/Fe_3O_4/C$ could possess an enhanced EMW absorption.

Details of the fabrication processes of the $Fe/Fe_3O_4/C$ composites are illustrated in Fig. 2. The prepared PS emulsion mentioned above was poured into the Fe_3O_4 solution under vigorous stirring for 1 h. Then the hybrid emulsion was filtered by a millipore filter and dried at 80 °C for 30 min in a nitrogen atmosphere to obtain the PS/Fe_3O_4 composite microspheres. The as-prepared PS/Fe_3O_4 composite microspheres were heated to 200 °C at a rate of 3 °C/min for 40 min and 90 min, respectively, to obtain a thermosetting property (the process is called pre-oxidation) in the ambient atmosphere. Then, the samples were heated to 900 °C for 30 min in a horizontally tubular furnace under flowing Ar atmosphere (flowing rate, 20 mL/min) to obtain the $Fe/Fe_3O_4/C$ monodispersed composite microspheres. Based on the different pre-oxidized time, the corresponding samples are denoted as $Fe/Fe_3O_4/C$-40 and $Fe/Fe_3O_4/C$-90, respectively.
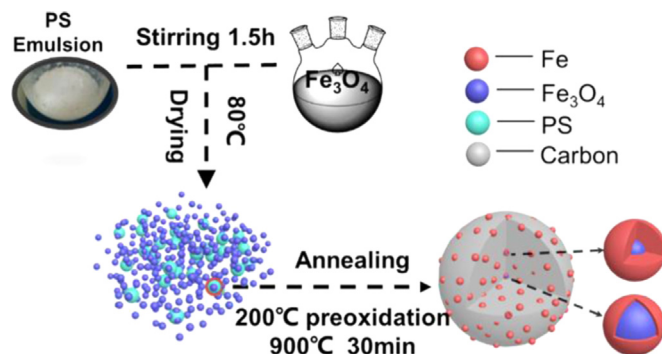

Fig. 2. Schematic illustration of the fabrication processes of the $Fe/Fe_3O_4/C$ composite microspheres.

2.2. Characterization methods

The microstructure images were obtained on a MX2600FE field emission scanning electron microscopy (SEM). The transmission electron microscope (TEM) images were collected on a Tecnai F30 FEG electron microscope equipped with an energy dispersive X-ray spectroscopy (EDS). X-ray diffraction (XRD) patterns of the as-synthesized samples were performed on a Rigaku D/Max 2000 VPC powder X-ray diffractometer operated at a voltage of 30 kV and current of 20 mA with Cu Kα radiation. The Raman spectra of the samples were achieved on a Renishaw RM-1000 Raman spectrometer with a 532 nm line from a laser excitation. EMW performances including the relative complex permittivity were determined on an Agilent N5245A vector network analyzer with transmission reflection mode in the frequency range of 2–18 GHz at room temperature. The composite specimens for RL measurements were pressed into a steel mold to shape a cylinder with the inner diameter of 3.0 mm, the outer diameter of 7.0 mm and the thickness of 2–4 mm by uniformly mixing the microspheres in a paraffin matrix in a mass ratio of 7:3.

3. Results and discussion

Fig. 3 shows the SEM images of the as-prepared PS microspheres which were synthesized at different molar ratios of styrene and ammonium persulfate (from 60:1 to 100:1 and from 1:0.009 to 1:0.018). Fig. 3a shows that the as-prepared PS microspheres exhibit a uniform morphology with the diameter about 0.8 μm and without obvious aggregation, when the products were synthesized at the molar ratio of 60:1 of styrene and ammonium persulfate. Fig. 3b illustrates the PS microspheres still retain the morphology of the monodispersed distribution with a diameter of 1 μm and without obvious aggregation. When the molar ratio of styrene and ammonium persulfate changed to 10:1, the uniformity of the products started to deteriorate and the diameter enlarged to ∼ 2 μm (Fig. 3c). The diameter of the products increases from 0.8 μm to 2 μm with the promotion of the ratio of styrene and ammonium persulfate from 60:1 to 100:1. The phenomenon indicates that excessive styrene monomers could accelerate the growth of PS microspheres due to abundant nucleus for nucleating and extending [35]. The SEM images of PS microspheres produced at the molar ratios 1:0.009, 1:0.014 and 1:0.018 of styrene and ammonium persulfate respectively are shown in Fig. 3d–f. It can be seen that the average diameters of the products are about 2 μm, 1 μm and 0.8 μm from Fig. 3d–f, respectively (the particle size decreases with the increase of ammonium persulfate). The phenomenon indicates that the excessive anions $S_2O_4^{2-}$ generated in the emulsion boosts the electrostatic repulsion between molecular groups, thereby, the stability of the nuclei is improved and the diameter of the products could be reduced [34]. Fig. 3f displays that chain-like PS particles are obtained, which is attributed to the lower pH value of the emulsion with the increased concentration of ammonium
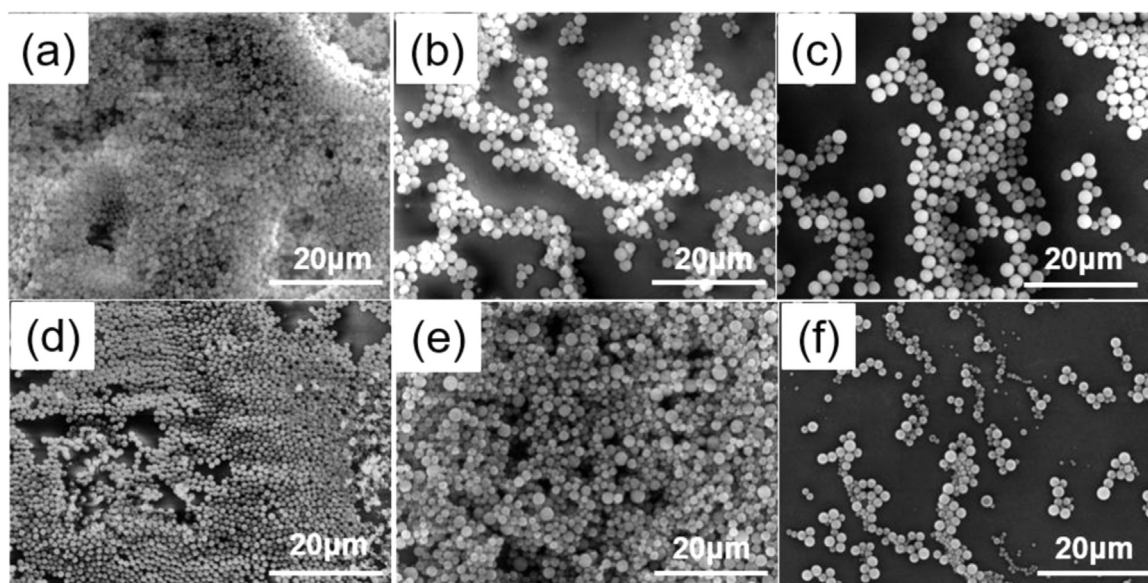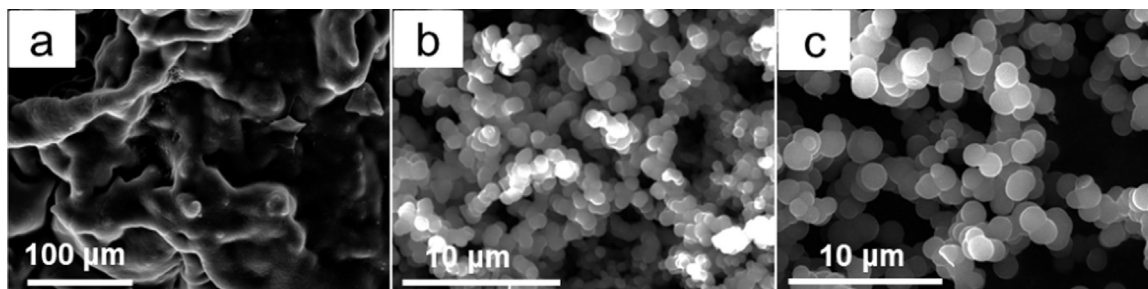
Fig. 3. The SEM images of the as-prepared PS microspheres which were synthesized at different molar ratio (a) 60:1; (b) 80:1; (c) 100:1; (d) 1:0.009; (e). 1:0.0140; (f) 1:0.0180 of styrene and ammonium persulfate.

persulfate [36].

The morphologies of the annealed products at 900 °C were characterized by SEM (Fig. 4), including the one without pre-oxidization process (Fig. 4a) and the other two with pre-oxidization process (Fig. 4b and c). All the products were obtained with the molar ratio 100: 1 of styrene and ammonium persulfate. Fig. 4a exhibits the products directly heated to 900 °C without pre-oxidation. The spherical morphology of the PS microspheres totally disappeared owing to the thermal adhesion and agglomeration during the heating process. Fig. 4b and c show the annealed products with a pre-oxidization process (versus Fig. 4a) at 200 °C for 40 min and 90 min, respectively. Fig. 4b shows that the spherical structure (diameter: $\sim 2\,\mu m$) of the annealed products is retained when the original PS microspheres are pre-oxidized for 40 min at 200 °C before annealing. The agglomeration phenomenon still exists due to a relative short preoxidation time. Fig. 4c exhibits the morphology of the sample pre-oxidized at 200 °C for 40 min and then annealed at 900 °C for 30 min. The products show intact spherical morphology and almost no agglomeration is observed owing to the longer pre-oxidation. The possible reason is that oxygen as crosslink reagent could sufficiently diffuse into the surface of PS microspheres and react with pendant groups, such as phenyls, to form a crosslinking chain (the transformation of thermoplastic to thermosetting occurs during the pre-oxidation process).

TEM was applied to further investigate the morphologies and structures of the as-synthesized carbon microspheres, Fe_3O_4 nanoparticles and $Fe/Fe_3O_4/C$-90 architectures. As shown in Fig. 5a, the low magnification TEM image of the annealed carbon microspheres (pre-

oxidized at 200 °C for 90 min then annealed at 900 °C for 30 min) exhibits the spherical and unfeatured morphology. Fig. 5b shows a bright field TEM image of the carbon microspheres which possesses a typical core-shell structure according to the high magnification TEM image (inset of Fig. 5b). The thickness of the shell layer is about 25 nm which would suggest the diffusion depth of oxygen during the pre-oxidation stage. The CO_2/CO gas would be released during the pre-oxidized process, which left defects and/or vacancies in the shell. In high temperature carbonization stage, these defects and vacancies are preserved forming the core-shell structure [37,38]. In Fig. 5c, the EDS spectrum (from the selected area in Fig. 5a) shows that only C element exists in the pre-oxidized PS microspheres sample indicating that the annealed PS microspheres are carbon microspheres virtually. The low (Fig. 5d) and high (Fig. 5e) magnification TEM images of the Fe_3O_4 nanoparticles illustrate that Fe_3O_4 nanoparticles are successfully fabricated without obvious agglomeration and the diameters of the Fe_3O_4 products are about 20 nm. Fig. 5f and g show the low and high magnification TEM images of $Fe/Fe_3O_4/C$-90 architectures, respectively. The large sphere is the carbon microspheres anchored by large numbers of Fe_3O_4 nanoparticles on the surface according to Fig. 5f. Fig. 5g shows the carbon microspheres are successfully coated by dense and uniform Fe_3O_4 nanoparticles. As shown in Fig. 5h, the EDS spectrum indicates that the main elements are C、Fe and O in the products. Fig. 5i (1–6) exhibits the digital photographs of $Fe/Fe_3O_4/C$-90 composite microspheres following a magnet. Fig. 5i-1 demonstrates that $Fe/Fe_3O_4/C$-90 architectures possess a prominent magnetism property. As presented in Fig. 5i (2–6), $Fe/Fe_3O_4/C$-90 architectures flow along with the magnet,

Fig. 4. The SEM images of PS microspheres prepared at the molar ratio 100: 1 (a) directly annealed at 900 °C without preoxidation; pre-oxidized at 200 °C for (b) 40 min and (c) 90 min before being annealed at 900 °C.
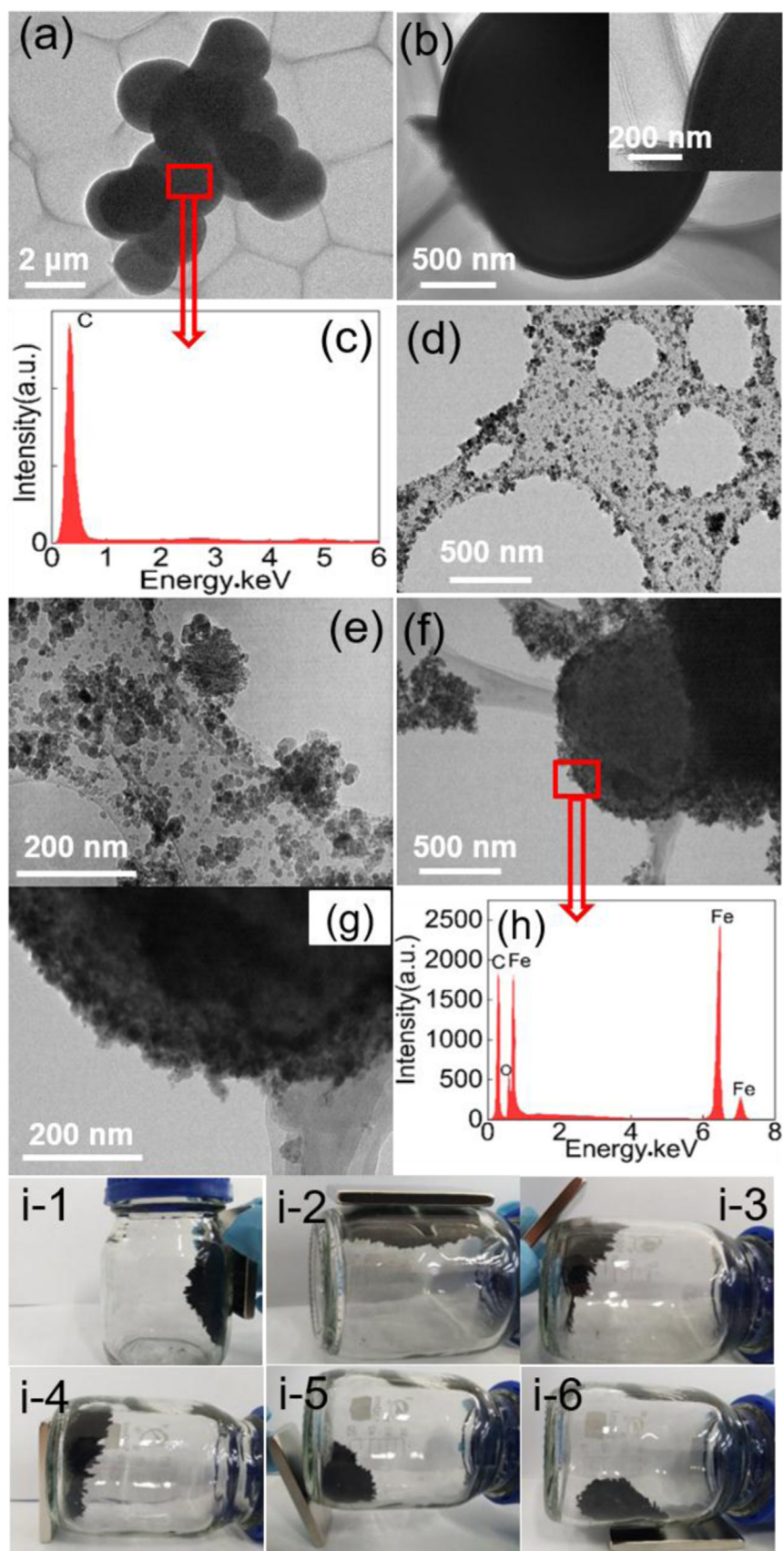
Fig. 5. The (a) low and (b) high magnification TEM image of the annealed PS microspheres pre-oxidized at 200 °C for 90 min before being annealed at 900 °C for 30 min; (c) the EDS spectrum of carbon microspheres; the (d) low and (e) high magnification TEM images of the Fe_3O_4 nanoparticles; the (f) low and (g) high magnification TEM images of the $Fe/Fe_3O_4/C$-90; (h) the EDS spectrum of the $Fe/Fe_3O_4/C$-90; (i1–6) the digital photographs of the $Fe/Fe_3O_4/C$-90 following a magnet.
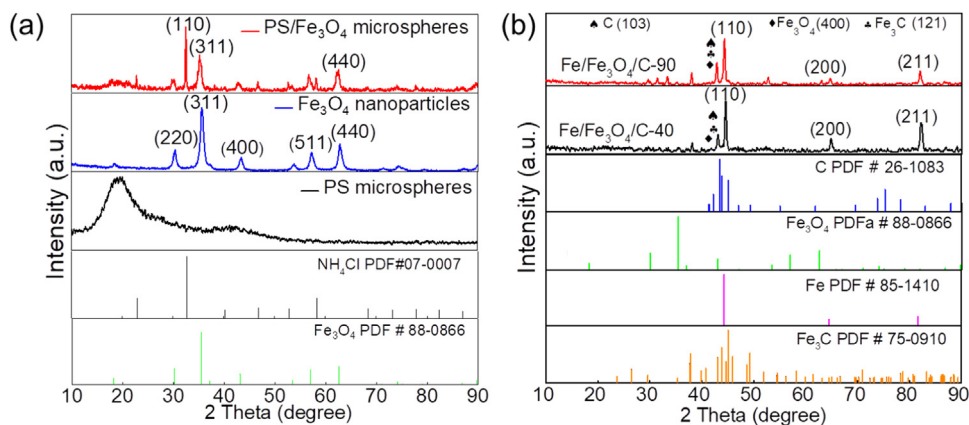
Fig. 6. XRD patterns of the (a) PS microspheres, the Fe₃O₄ nanoparticles and the PS/Fe₃O₄ composite microspheres; XRD patterns of (b) Fe/Fe₃O₄/C-40 and Fe/Fe₃O₄/C-90.

which indicates the superb flowability of the composite microspheres.

The XRD patterns of the PS microspheres, Fe₃O₄ nanoparticles and PS/Fe₃O₄ composite microspheres are shown in Fig. 6a. For PS microspheres, the pattern shows an extremely wide amorphous peak at about $2\theta = 19.4°$, which indicates PS microspheres possess an amorphous structure. For Fe₃O₄ nanoparticles, the diffraction peaks at $2\theta = 30.2$, 35.5, 43.2, 57.1 and 62.8° can be assigned to the planes of (220), (311), (400), (511) and (440), respectively, which demonstrates the presence of Fe₃O₄ (JCPDF no. 88-0866) [39]. The crystallite size of the as-prepared Fe₃O₄ was calculated by the Debye-Scherrer equation [16,40]:

$$D = \frac{k\lambda}{\beta\cos\theta}$$

(4)

where D is the crystallite size, k is a constant (equal to 0.9), λ is the wavelength of X-ray ($\lambda = 0.154$), β is the full width at half-maximum, θ is the diffraction angle. The calculated crystallite size of the as-prepared Fe₃O₄ is about 14 nm. The XRD pattern of the PS/Fe₃O₄ composite microspheres illustrates the typical peaks at $2\theta = 18.8°$, 32.4°, 35.2° and 62.5° corresponding to the amorphous structure of PS microspheres, the (110) plane of NH₄Cl, the (311) and (440) plane of Fe₃O₄ nanoparticles, respectively [JCPDF no. 07-0007]. The existence of NH₄Cl is caused by ammonia water which was added in the solution to adjust the pH. The XRD patterns of Fe/Fe₃O₄/C-40 and Fe/Fe₃O₄/C-90 are shown in Fig. 6b. The diffraction peaks at $2\theta = 44.5°$, 65.0° and 82.4° shown in the patterns can be indexed to the planes of (110), (200) and (211) of Fe, respectively (JCPDS no. 85-1410) [16], because of the reduction of Fe₃O₄ to Fe during the thermal carbonization process. The crystallite size of the as-prepared Fe is 26 nm which was calculated by the aforementioned Debye-Scherrer equation. Fe₃C (the (121) planes) can be detected due to the typical diffusion of C atoms into Fe₃O₄ particles and the carbothermal reduction reaction [41,42].

The Raman spectra of the prepared Fe/Fe₃O₄/C-40 and Fe/Fe₃O₄/C-90 is shown in Fig. 7. The typical vibrations peaks at the wavenumber 1342.3 cm⁻¹ and 1598.5 cm⁻¹ attribute to the D-band and G-band, respectively. D-band is related to the sp³ defects or lattice distortion [43], which could be attributed to disordered structures of carbon originated from vacancies, amorphous carbon species and/or lattice defects [27,44]. The G-band is attributed to the stretching of sp²-bonded C-C pairs [45]. A broad peak from 2467.5 to 2928.1 cm⁻¹ can be assigned to the 2D-band that indicates the number of multiple layers structure of carbon according to its relative intensity with respect to the G band and its position [46,47]. The intensity ratio value of D band to G band (I_D/I_G) representing the degree of disorder in the graphite structure [7] decreases from 0.892 for 40 min to 0.832 for 90 min, which indicates the transformation of amorphous carbon to ordered sp² graphical structure at the assistance of high temperature [48].

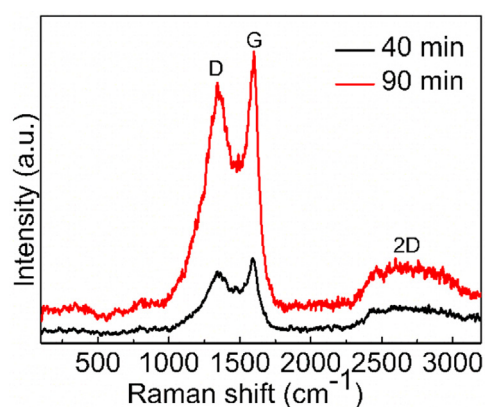As for the experiments, a possible reaction mechanism for the

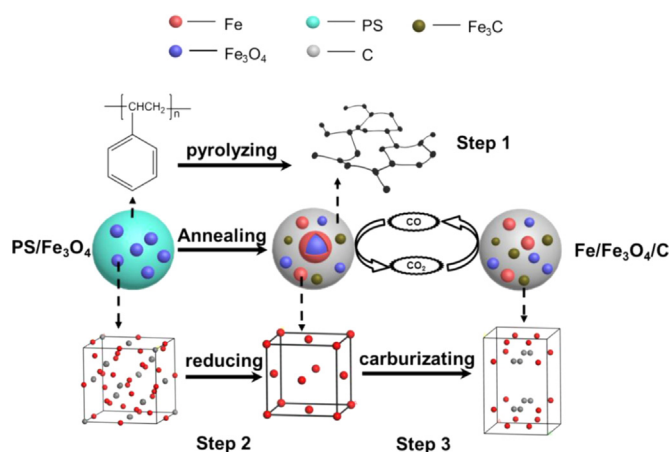**Fig. 7.** The Raman spectrum of as-prepared samples annealed at 900 °C for 40 min and 90 min respectively.

Fig. 8. The schematic representation of the evolution of carbothermal reduction process.

formation of the Fe/Fe₃O₄/C is proposed. As illustrated in Fig. 8, the procedure of the evolution of the Fe/Fe₃O₄/C could be divided into three steps. In the first step, we propose that PS microspheres convert into carbon structure by releasing small volatile molecules, which might include HCl, methylbenzene and ethylbenzene. In the second step, we conclude that Fe₃O₄ particles are reduced by as-generated carbon to Fe [30], as showing below in Eq. (5)

$$Fe_3O_4 + C \rightarrow Fe + CO_2\uparrow$$

(5)

In the third step, we propose that C atoms diffuse into the
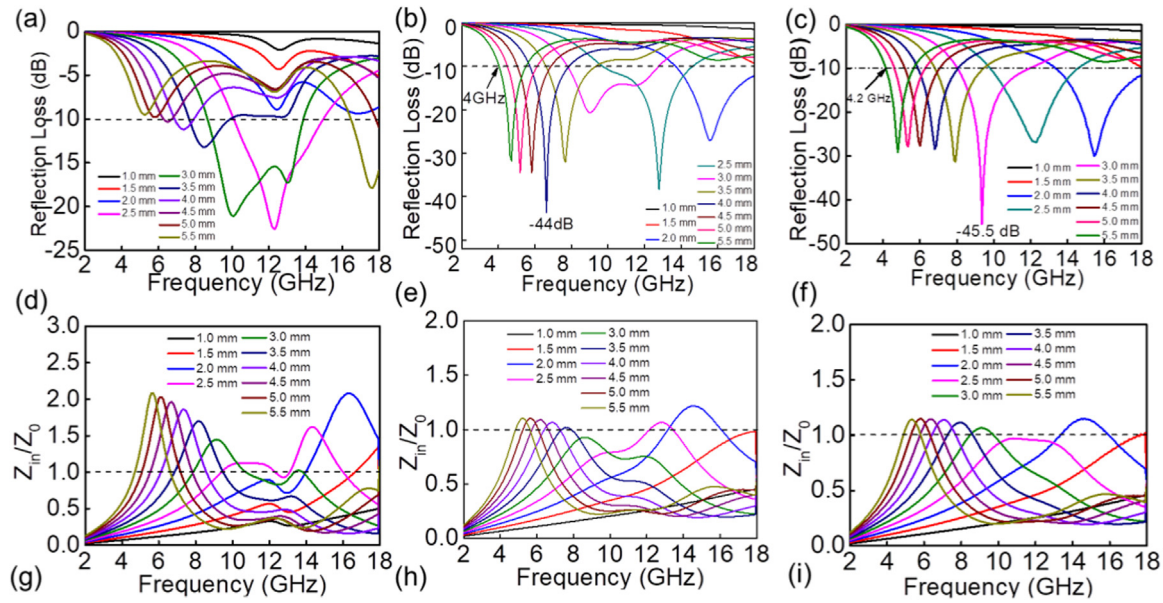
Fig. 9. The reflection loss of the (a) carbon microspheres; (b) Fe/Fe$_3$O$_4$/C-40; and (c) Fe/Fe$_3$O$_4$/C-90 with the different thicknesses in the 2–18 GHz; the curve of Z$_{in}$/Z$_0$ of the (d) carbon microspheres; (e) Fe/Fe$_3$O$_4$/C-40; and (f) Fe/Fe$_3$O$_4$/C-90 with the different thicknesses.

octahedral interstice of cubic Fe lattice during the carbothermal reaction [49]. An equation for the reduction may be described as follows:

$$3Fe + C \rightarrow Fe_3C \tag{6}$$

The reflection loss (RL) of the pure carbon microspheres (Fig. 9a), Fe/Fe$_3$O$_4$/C-40 (Fig. 9b) and Fe/Fe$_3$O$_4$/C-90 (Fig. 9c) is shown in the range of 2–18 GHz, respectively. As shown in Fig. 9a, the minimum RL value of the carbon microspheres is − 23 dB at 12.3 GHz with a sample thickness of 2.5 mm and the effective absorption bandwidth (below − 10 dB) is 8.8 GHz from 6.2 to 15.0 GHz. Fig. 9b exhibits the reflection loss of Fe/Fe$_3$O$_4$/C-40. It can be observed that the minimum RL is − 44 dB at 6.6 GHz, and the effective bandwidth (below − 10 dB) can reach up to 14.0 GHz from 4.0 to 18.0 GHz, which indicates an excellent absorption for lower frequency EMW. An outstanding effective bandwidth (below − 10 dB) in the lower frequency range of 4–8 GHz indicates the practical value for new generation stealth materials. For Fe/Fe$_3$O$_4$/C-90, as shown in Fig. 9c, the minimum RL value shifts to lower frequency with larger thickness, and the minimum RL can reach − 45.5 dB at 9.4 GHz with the effective absorption bandwidth of 13.8 GHz (4.2–18 GHz). It should be noticed that Z$_{in}$/Z$_0$ = 1 is critical to realize ideal impedance matching, which indicates that subtotal EMW permeates the composite samples and can be attenuated extremely. To explore the relationship between the impedance matching and the RL value, the Z$_{in}$/Z$_0$ value of the pure carbon microspheres (Fig. 9d), Fe/Fe$_3$O$_4$/C-40 (Fig. 9e) and Fe/Fe$_3$O$_4$/C-90 (Fig. 9f) is analyzed. As shown in Fig. 9d, the Z$_{in}$/Z$_0$ value of the pure carbon microspheres is far from 1, which demonstrates the impedance matching of the pure carbon microspheres is inferior. The Z$_{in}$/Z$_0$ value of Fe/Fe$_3$O$_4$/C-40 is shown in Fig. 9e. The Z$_{in}$/Z$_0$ value is close to 1, which indicates that the impedance matching is improved. Particularly, when the thickness of Fe/Fe$_3$O$_4$/C-40 is 2.0 mm, the Z$_{in}$/Z$_0$ value is roughly equal to 1 and the RL value reaches the minimum value (Fig. 9b). The Z$_{in}$/Z$_0$ curve of Fe/Fe$_3$O$_4$/C-90 with the different thicknesses is shown in Fig. 9f. Fig. 9f shows that the Z$_{in}$/Z$_0$ value is closest to 1 and the minimum RL value is obtained (Fig. 9c), when the thickness of Fe/Fe$_3$O$_4$/C-90 is 3.0 mm. Compared to the pure carbon microspheres, the impedance matching of Fe/Fe$_3$O$_4$/C-40 and Fe/Fe$_3$O$_4$/C-90 is improved. The RL is enhanced by the composite structure of the Fe/Fe$_3$O$_4$/C in which carbon microspheres contribute to dielectric loss, and Fe and Fe$_3$O$_4$ contribute to magnetic loss and electromagnetic impedance matching as we cogitatively designed.

The effective complex permittivity (ε_r) is examined to measure the EMW absorption performance. The real part of the complex permittivity (ε') is related to the stored energy, and the imaginary part of the complex permittivity (ε'') represents the attenuation capability of electric and magnetic energies [50–52]. The real part ε' and the imaginary part ε'' of the complex permittivity of the carbon microspheres, Fe/Fe$_3$O$_4$/C-40 and Fe/Fe$_3$O$_4$/C-90 are shown in Fig. 10a and b, respectively. It can be seen that Fe/Fe$_3$O$_4$/C-40 and Fe/Fe$_3$O$_4$/C-90 exhibit larger values of ε' and ε'' than that of the carbon microspheres (derived from PS microspheres), which could originate from the improvement of the polarization of magnetic domains in the Fe$_3$O$_4$ [53,54]. The complex permittivity of all the samples are declined with the promotion of frequency, which is attributed to the hysteresis of the induction charge and the decrease of the space charge polarization [55]. A significant fluctuation at the range of 12–13 GHz could imply a local inhomogeneity of the defects in the three samples [56]. The dielectric loss tangent (tan $\delta_e = \varepsilon''/\varepsilon'$) is another parameter to control the enhancement of absorption. Fig. 10c depicts that the dielectric loss tangent values of the composites are higher than the carbon spheres, which indicates the interfacial polarization of the Fe/Fe$_3$O$_4$/C in accordance with the above simulation results.

In order to exam the polydispersive nature of dielectric relaxation, Cole-Cole plots are shown in Fig. 10d–f, which can illustrate the complex Argand plane plot of ε'' and ε' ($\varepsilon = \varepsilon' + i\varepsilon''$). The real ($\varepsilon'$) and imaginary ($\varepsilon''$) part of the complex permittivity are given as [20,53]:

$$\varepsilon' = \varepsilon_\infty + \frac{\varepsilon_s - \varepsilon_\infty}{1 + \omega^2\tau^2} \tag{7}$$

$$\varepsilon'' = \frac{(\varepsilon_s - \varepsilon_\infty)\omega\tau}{1 + \omega^2\tau^2} \tag{8}$$

where ε_s is static permittivity and ε_∞ is permittivity which is the limit value during the process with the change of ω, ω is frequency, τ is polarization relaxation period.

The Cole-Cole semicircle (Debye semicircle) is obtained to eliminate $\omega\tau$ according to Eqs. (7) and (8), which is described as:

$$\left[\varepsilon' - \frac{1}{2}(\varepsilon_s - \varepsilon_\infty)\right]^2 + (\varepsilon'')^2 = \frac{1}{4}(\varepsilon_s + \varepsilon_\infty)^2 \tag{9}$$

A semicircle indicates a Debye relaxation process, indicating the departure of electrical response. Fig. 10d–f show the curves of Cole-Cole
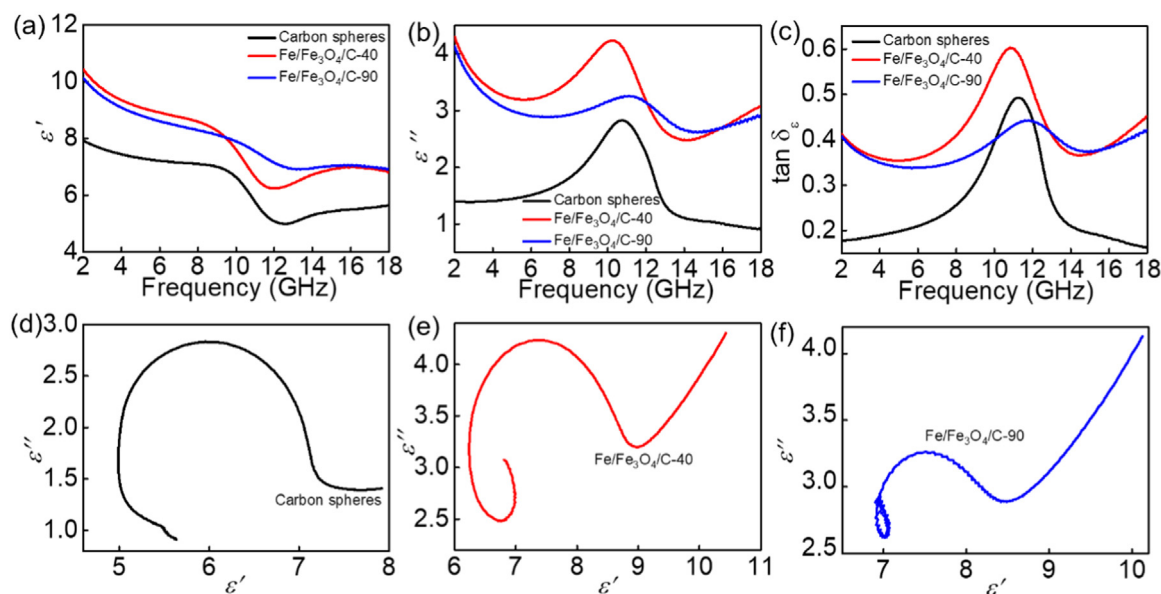
Fig. 10. The (a) real part ε′. and the (b) imaginary part ε″. of the complex permittivity and (c) the dielectric loss tangent tan δ_ε and (d–f) Cole-Cole (ε″-ε′) of the carbon microspheres, Fe/Fe₃O₄/C-40 and Fe/Fe₃O₄/C-90, respectively.

of the carbon microspheres, Fe/Fe$_3$O$_4$/C-40 and Fe/Fe$_3$O$_4$/C-90, respectively. Only one semicircle of the carbon microspheres is observed in Fig. 10d. Compared to the carbon microspheres, as shown in Fig. 10e and f, both of Cole-Cole plots of Fe/Fe$_3$O$_4$/C-40 and Fe/Fe$_3$O$_4$/C-90 show multiple semicircles, which could manifest that new relaxation processes have been induced into Fe/Fe$_3$O$_4$/C system. In both cases, the relaxation behavior could deviate from classical Debye type considering that all of the centers of semicircles obviously lie below the real axis (ε′) [34,57]. Combining the aforementioned analyses of SEM and TEM, the core-shell structure formed in Fe/Fe$_3$O$_4$/C-40 and Fe/Fe$_3$O$_4$/C-90 versus carbon microspheres, which means that more defects and vacancies in/on the Fe/Fe$_3$O$_4$/C system leading to the short-range hopping of the ions, facilitating interfacial relaxation and further promoting EMW dissipation. Furthermore, during the carbothermal reduction reaction, the Fe/Fe$_3$O$_4$/C can generate some vacancies on account of CO_2 giving off. The introduced Fe$_3$O$_4$ nanoparticles could improve the magnetic loss of the Fe/Fe$_3$O$_4$/C and accelerate the energy loss to enhance the EMW absorption ability [54]. Moreover, the heterogeneous mixtures including samples and paraffin influence the relaxation of electromagnetic wave [20]. The displacement current lag attributes to the further polarization relaxation at the core-shell interface structure (see Fig. 5b) among the alternating EMW field [58]. In summary, all of relaxation processes facilitate to enhance the reflection losses.

4. Conclusion

In summary, novel monodispersed Fe/Fe$_3$O$_4$/C composite microspheres was prepared successfully by carbonizing PS/Fe$_3$O$_4$ microspheres in a tube furnace. The morphology evolution of the products, crystalline size and phase structures, preoxidation processes, and the EMW absorption properties are systematically studied. The Fe/Fe$_3$O$_4$/C-90 composite microspheres exhibit a uniform diameter about 2 µm with an enhanced EMW absorption from the minimum RL −45.5 dB at 9.4 GHz with a bandwidth of −4.03 dB at a thickness of 3.0 mm. The effective EMW absorption bands can be tailored by the collaboration of the carbon microspheres, Fe/Fe$_3$O$_4$/C-40 and Fe/Fe$_3$O$_4$/C-90. The products also have an outstanding flowability which could be a candidate for next generation stealth materials (especially critical Mach number aerocraft) and industrial shielding materials.

References

[1] Y. Lin, J. Dai, H. Yang, L. Wang, F. Wang, Graphene multilayered sheets assembled by porous Bi$_2$Fe$_4$O$_9$ microspheres and the excellent electromagnetic wave absorption properties, Chem. Eng. J. 334 (2018) 1740–1748.

[2] B. Kuang, W. Song, M. Ning, J. Li, Z. Zhao, D. Guo, M. Cao, H. Jin, Chemical reduction dependent dielectric properties and dielectric loss mechanism of reduced graphene oxide, Carbon 127 (2018) 209–217.

[3] J. Xi, E. Zhou, Y. Liu, W. Gao, J. Ying, Z. Chen, C. Gao, Wood-based straightway channel structure for high performance microwave absorption, Carbon 124 (2017) 492–498.

[4] X. Qiu, L. Wang, H. Zhu, Y. Guan, Q. Zhang, Lightweight and efficient microwave absorbing materials based on walnut shell-derived nano-porous carbon, Nanoscale 9 (22) (2017) 7408–7418.

[5] S. Xie, Z. Ji, Y. Yang, G. Hou, J. Wang, Electromagnetic wave absorption enhancement of carbon black/gypsum based composites filled with expanded perlite, Compos. Part B: Eng. 106 (2016) 10–19.

[6] Y. Ding, Q. Liao, S. Liu, H. Guo, Y. Sun, G. Zhang, Y. Zhang, Reduced graphene oxide functionalized with cobalt ferrite nanocomposites for enhanced efficient and lightweight electromagnetic wave absorption, Sci. Rep. 6 (2016) 32381.

[7] R. Qiang, Y. Du, H. Zhao, Y. Wang, C. Tian, Z. Li, X. Han, P. Xu, Metal organic framework-derived Fe/C nanocubes toward efficient microwave absorption, J. Mater. Chem. A 3 (25) (2015) 13426–13434.

[8] Y. Zhang, Y. Huang, H. Chen, Z. Huang, Y. Yang, P. Xiao, Y. Zhou, Y. Chen, Composition and structure control of ultralight graphene foam for high-performance microwave absorption, Carbon 105 (2016) 438–447.

[9] B. Zhong, Y. Cheng, M. Wang, Y. Bai, X. Huang, Y. Yu, H. Wang, G. Wen, Three dimensional hexagonal boron nitride nanosheet/carbon nanotube composites with light weight and enhanced microwave absorption performance, Compos. Part A: Appl. Sci. Manuf. 112 (2018) 515–524.

[10] J. Li, W. Lu, J. Suhr, H. Chen, J.Q. Xiao, T.W. Chou, Superb electromagnetic wave-absorbing composites based on large-scale graphene and carbon nanotube films, Sci. Rep. 7 (1) (2017) 2349.

[11] Y. Wang, W. Wang, J. Sun, C. Sun, Y. Feng, Z. Li, Microwave-based preparation and characterization of Fe-cored carbon nanocapsules with novel stability and super electromagnetic wave absorption performance, Carbon 135 (2018) 1–11.

[12] S.K. Singh, H. Prakash, M.J. Akhtar, K.K. Kar, Lightweight and high-performance microwave absorbing heteroatom-doped carbon derived from chicken feather fibers, ACS Sustain. Chem. Eng. 6 (4) (2018) 5381–5393.

[13] T. Zhao, C. Hou, H. Zhang, R. Zhu, S. She, J. Wang, T. Li, Z. Liu, B. Wei, Electromagnetic wave absorbing properties of amorphous carbon nanotubes, Sci.

Rep. 4 (2014) 5619.

[14] L. Yang, L. Tong, Suspended monolayer graphene traps high-speed single-walled carbon nanotube, Carbon 107 (2016) 689–695.

[15] H. Wang, D. Zhu, W. Zhou, F. Luo, Effect of multiwalled carbon nanotubes on the electromagnetic interference shielding properties of polyimide/carbonyl iron composites, Ind. Eng. Chem. Res. 54 (25) (2015) 6589–6595.

[16] B. Qu, C. Zhu, C. Li, X. Zhang, Y. Chen, Coupling hollow Fe_3O_4-Fe nanoparticles with graphene sheets for high-performance electromagnetic wave absorbing material, ACS Appl. Mater. Interfaces 8 (6) (2016) 3730–3735.

[17] F. Yan, D. Guo, S. Zhang, C. Li, C. Zhu, X. Zhang, Y. Chen, An ultra-small $NiFe_2O_4$ hollow particle/graphene hybrid: fabrication and electromagnetic wave absorption property, Nanoscale (2018).

[18] Y. Yin, M. Zeng, J. Liu, W. Tang, H. Dong, R. Xia, R. Yu, Enhanced high-frequency absorption of anisotropic Fe_3O_4/graphene nanocomposites, Sci. Rep. 6 (2016) 25075.

[19] Y. Li, M. Yu, P. Yang, J. Fu, Enhanced microwave absorption property of fe nanoparticles encapsulated within reduced graphene oxide with different thicknesses, Ind. Eng. Chem. Res. 56 (31) (2017) 8872–8879.

[20] G. Shen, B. Mei, H. Wu, H. Wei, X. Fang, Y. Xu, Microwave electromagnetic and absorption properties of N-doped ordered mesoporous carbon decorated with ferrite nanoparticles, J. Phys. Chem. C 121 (7) (2017) 3846–3853.

[21] L. Wang, Y. Guan, X. Qiu, H. Zhu, S. Pan, M. Yu, Q. Zhang, Efficient ferrite/Co/ porous carbon microwave absorbing material based on ferrite@metal–organic framework, Chem. Eng. J. 326 (2017) 945–955.

[22] H. Jiang, F. Zhao, S. Zang, Magnetically recoverable B,F,P-TiO_2/Fe_3O_4 nanophotocatalyst with enhanced charge separation efficiency, Mater. Sci. Semicond. Process. 75 (2018) 103–111.

[23] Y. Huang, C.-f. Xiao, Q.-l. Huang, H.-l. Liu, J.-q. Hao, L. Song, Magnetic field induced orderly arrangement of Fe_3O_4/GO composite particles for preparation of Fe_3O_4/GO/PVDF membrane, J. Membr. Sci. 548 (2018) 184–193.

[24] Y. Shao, W. Lu, H. Chen, J.Q. Xiao, Y. Qiu, T.-W. Chou, Flexible ultra-thin Fe_3O_4/ MnO_2 core-shell decorated CNT composite with enhanced electromagnetic wave absorption performance, Compos. Part B: Eng. (2018).

[25] S.H. Hosseini, S.H. Mohseni, A. Asadnia, H. Kerdari, Synthesis and microwave absorbing properties of polyaniline/$MnFe_2O_4$ nanocomposite, J. Alloy. Compd. 509 (14) (2011) 4682–4687.

[26] D. Sun, Q. Zou, Y. Wang, Y. Wang, W. Jiang, F. Li, Controllable synthesis of porous Fe_3O_4@ZnO sphere decorated graphene for extraordinary electromagnetic wave absorption, Nanoscale 6 (12) (2014) 6557–6562.

[27] W. Li, B. Lv, L. Wang, G. Li, Y. Xu, Fabrication of Fe_3O_4@C core–shell nanotubes and their application as a lightweight microwave absorbent, RSC Adv. 4 (99) (2014) 55738–55744.

[28] X. Liu, Y. Chen, X. Cui, M. Zeng, R. Yu, G.-S. Wang, Flexible nanocomposites with enhanced microwave absorption properties based on Fe_3O_4/SiO_2 nanorods and polyvinylidene fluoride, J. Mater. Chem. A 3 (23) (2015) 12197–12204.

[29] X. Zhang, W.-H. Gui, Q. Zeng, Q. Chen, Vibrational and dielectric properties of AlN: a first-principles study, Ceram. Int. 42 (16) (2016) 18828–18832.

[30] G. Wu, Y. Cheng, Z. Yang, Z. Jia, H. Wu, L. Yang, H. Li, P. Guo, H. Lv, Design of carbon sphere/magnetic quantum dots with tunable phase compositions and boost dielectric loss behavior, Chem. Eng. J. 333 (2018) 519–528.

[31] D. Li, D. Yu, B. Xu, J. He, Z. Liu, P. Wang, Y. Tian, Synthesis of semimetallic $BC_{3.3}N$ with orthorhombic structure at high pressure and temperature, Cryst. Growth 8 (7) (2008) 2096–2100.

[32] X. Lu, X. Gao, C. Li, J. Ren, X. Guo, P. La, Electronic structure and optical properties of doped gallium phosphide: a first-principles simulation, Phys. Lett. A 381 (35) (2017) 2986–2992.

[33] J.Y. Yang, L.H. Liu, J.Y. Tan, First-principles study on dielectric function of isolated and bundled carbon nanotubes, J. Quant. Spectrosc. Radiat. Transf. 158 (2015) 78–83.

[34] T. Zhang, J. Zhang, G. Wen, B. Zhong, L. Xia, X. Huang, H. Zhao, H. Wang, L. Qin, Ultra-light h-BCN architectures derived from new organic monomer with tunable electromagnetic wave absorption, Carbon 136 (2018) 345–358.

[35] J. Cui, C. Zhu, M. He, Z. Ke, Y. Liu, Q. Tai, X. Xiao, Y. Hu, Preparation of a novel styrene copolymer: simultaneously improving the thermal stability and toughness, J. Appl. Polym. Sci. 135 (16) (2018) 46120.

[36] F. Zhang, Y. Bai, Y. Ma, W. Yang, Preparing of monodisperse and cation-charged polystyrene particles stabilized with polymerizable quarternary ammonium by dispersion polymerization in a methanol-water medium, J. Colloid Interface Sci.

[37] Y. Liu, Y. Ma, L. Liu, W. Yang, Facile synthesis of core-shell/hollow anisotropic particles via control of cross-linking during one-pot dispersion polymerization, J. Colloid Interface Sci. 445 (2015) 268–276.

[38] S. Wang, K. Yue, L. Liu, W. Yang, Photoreactive, core-shell cross-linked/hollow microspheres prepared by delayed addition of cross-linker in dispersion polymerization for antifouling and immobilization of protein, J. Colloid Interface Sci. 389 (1) (2013) 126–133.

[39] X. Lu, Y. Wu, H. Cai, X. Qu, L. Ni, C. Teng, Y. Zhu, L. Jiang, Fe_3O_4 nanopearl decorated carbon nanotubes stemming from carbon onions with self-cleaning and microwave absorption properties, RSC Adv. 5 (67) (2015) 54175–54181.

[40] A. Jafari, S. Farjami Shayesteh, M. Salouti, K. Boustani, Effect of annealing temperature on magnetic phase transition in Fe_3O_4 nanoparticles, J. Magn. Magn. Mater. 379 (2015) 305–312.

[41] L. Niu, X. Liu, X. Liu, Z. Lv, C. Zhang, Y. Wen, Y. Li, J. Xu, In situ XRD study on promotional effect of potassium on carburization of spray-dried precipitated Fe_2O_3 catalysts, ChemCatChem 9 (9) (2017) 1691–1700.

[42] Z. Cao, M. Qin, C. Zuo, Y. Gu, B. Jia, Facile route for synthesis of mesoporous graphite encapsulated iron carbide/iron nanosheet composites and their electrocatalytic activity, J. Colloid Interface Sci. 491 (2017) 55–63.

[43] C.N.R. Rao, K. Gopalakrishnan, A. Govindaraj, Synthesis, properties and applications of graphene doped with boron, nitrogen and other elements, Nano Today 9 (3) (2014) 324–343.

[44] P. Wang, L. Cheng, Y. Zhang, L. Zhang, Synthesis of SiC nanofibers with superior electromagnetic wave absorption performance by electrospinning, J. Alloy. Compd. 716 (2017) 306–320.

[45] S. Acharya, J. Ray, T.U. Patro, P. Alegaonkar, S. Datar, Microwave absorption properties of reduced graphene oxide strontium hexaferrite/poly(methyl methacrylate) composites, Nanotechnology 29 (11) (2018) 115605.

[46] X. Li, W. Cai, J. An, S. Kim, J. Nah, D. Yang, R. Piner, A. Velamakanni, I. Jung, E. Tutuc, S.K. Banerjee, L. Colombo, R.S. Ruoff, Large-area synthesis of high-quality and uniform graphene films on copper foils, Science 324 (5932) (2009) 1312–1314.

[47] B. Liang, S. Wang, D. Kuang, L. Hou, B. Yu, L. Lin, L. Deng, H. Huang, J. He, Facile synthesis and excellent microwave absorption properties of FeCo-C core-shell nanoparticles, Nanotechnology 29 (8) (2018) 085604.

[48] P. Wang, L. Cheng, Y. Zhang, W. Yuan, H. Pan, H. Wu, Electrospinning of graphite/ SiC hybrid nanowires with tunable dielectric and microwave absorption characteristics, Compos. Part A: Appl. Sci. Manuf. 104 (2018) 68–80.

[49] K. Zhu, C. Chen, M. Xu, K. Chen, X. Tan, M. Wakeel, N.S. Alharbi, In situ carbothermal reduction synthesis of Fe nanocrystals embedded into N-doped carbon nanospheres for highly efficient U(VI) adsorption and reduction, Chem. Eng. J. 331 (2018) 395–405.

[50] M. González, J. Baselga, J. Pozuelo, High porosity scaffold composites of graphene and carbon nanotubes as microwave absorbing materials, J. Mater. Chem. C 4 (36) (2016) 8575–8582.

[51] H. Lv, G. Ji, W. Liu, H. Zhang, Y. Du, Achieving hierarchical hollow carbon@Fe@ Fe_3O_4 nanospheres with superior microwave absorption properties and lightweight features, J. Mater. Chem. C 3 (39) (2015) 10232–10241.

[52] M. Crespo, N. Méndez, M. González, J. Baselga, J. Pozuelo, Synergistic effect of magnetite nanoparticles and carbon nanofibres in electromagnetic absorbing composites, Carbon 74 (2014) 63–72.

[53] Y. Chen, A. Zhang, L. Ding, Y. Liu, H. Lu, A three-dimensional absorber hybrid with polar oxygen functional groups of MWNTs/graphene with enhanced microwave absorbing properties, Compos. Part B: Eng. 108 (2017) 386–392.

[54] N. Zhou, Q. An, Z. Xiao, S. Zhai, Z. Shi, Rational design of superior microwave shielding composites employing synergy of encapsulating character of alginate hydrogels and task-specific components (Ni NPs, Fe_3O_4/CNTs), ACS Sustain. Chem. Eng. 5 (6) (2017) 5394–5407.

[55] Y. Zheng, X. Wang, S. Wei, B. Zhang, M. Yu, W. Zhao, J. Liu, Fabrication of porous graphene-Fe_3O_4 hybrid composites with outstanding microwave absorption performance, Compos. Part A: Appl. Sci. Manuf. 95 (2017) 237–247.

[56] C. Chen, J. Xi, E. Zhou, L. Peng, Z. Chen, C. Gao, Porous graphene microflowers for high-performance microwave absorption, Nano-Micro Lett. 10 (2) (2017).

[57] A. Jaiswal, R. Das, T. Maity, P. Poddar, Dielectric and spin relaxation behaviour in $DyFeO_3$ nanocrystals, J. Appl. Phys. 110 (12) (2011) 124301.

[58] X. Liu, Y. Ma, Q. Zhang, Z. Zheng, L.-S. Wang, D.-L. Peng, Facile synthesis of Fe_3O_4/ C composites for broadband microwave absorption properties, Appl. Surf. Sci. 445 (2018) 82–88.